# Source-receiver Marchenko redatuming: Obtaining virtual receivers and virtual sources in the subsurface

Satyan Singh[1] and Roel Snieder[1]

## ABSTRACT

By solving the Marchenko equations, one can retrieve the Green's function (Marchenko Green's function) between a virtual receiver in the subsurface and points at the surface (no physical receiver is required at the virtual location). We extend the idea behind these equations to retrieve the Green's function between any two points in the subsurface, i.e., between a virtual source and a virtual receiver (no physical source or physical receiver is required at either of these locations). This Green's function is called the virtual Green's function, and it includes all primary, internal, and free-surface multiples. Similar to the Marchenko Green's function, this virtual Green's function requires the reflection response at the surface (single-sided illumination) and an estimate of the first-arrival traveltime from the virtual locations to the surface. These Green's functions can be used to image the interfaces from above and below.

## INTRODUCTION

In this paper, we retrieve the Green's function between two points in the subsurface of the earth. We call these two points a virtual source and a virtual receiver pair. To retrieve the Green's function at a virtual receiver for a virtual source, we require neither a physical source nor a physical receiver at the virtual source and receiver location. The requirements for the retrieval of this Green's function are the reflection response for colocated physical sources and physical receivers at the surface (single-sided illumination) and a smooth version of the velocity model (no small-scale details of the model are necessary). For brevity, we define this Green's function, i.e., the response of a virtual source recorded by a virtual receiver, as the virtual Green's function.

Similar ideas of retrieving Green's function between two points have been proposed, notably, in seismic interferometry (Wapenaar, 2004; Bakulin and Calvert, 2006; Curtis et al., 2006, 2009; van Manen et al., 2006; Snieder et al., 2007; Curtis and Halliday, 2010) and in the Marchenko method (Broggini and Snieder, 2012; Broggini et al., 2012; Wapenaar et al., 2013, 2014; Slob et al., 2014; Singh et al., 2015, 2016). However, these methods (interferometry and the Marchenko method) have more restrictions in the source-receiver geometry, as discussed later, for the accurate retrieval of Green's function than our proposed method.

In seismic interferometry, we create virtual sources at locations where there are physical receivers. We also require a closed surface of sources to adequately retrieve the Green's function. Unlike interferometry, a physical receiver or physical source is not needed by our method to create either a virtual source or a virtual receiver, and we only require single-sided illumination (a closed surface of sources is not needed). The Green's function retrieved by the Marchenko equations is the response to a virtual source in the subsurface recorded by physical receivers at the surface (Broggini and Snieder, 2012; Broggini et al., 2012; Wapenaar et al., 2013, 2014; Slob et al., 2014; Singh et al., 2015, 2016). The Marchenko retrieved Green's function requires neither a physical source nor a physical receiver at the virtual source location in the subsurface.

Our algorithm retrieves the Green's function (upgoing and downgoing at the receiver) for virtual sources and virtual receivers. The Marchenko-retrieved Green's functions are limited to virtual sources in the subsurface recorded at the surface, but our algorithm presented in this paper is not restricted to recording on the surface for each virtual source. In our method, the response of the virtual source can be retrieved for a virtual reciever anywhere in the subsurface.

Wapenaar et al. (2016) propose similar work to ours; however, our derivation of the Green's function between two arbitrary points in the subsurface is used for imaging the subsurface with the up- and downgoing virtual Green's functions.

In this paper, we discuss the theory of retrieving the virtual Green's function. Our numerical examples are split into three sections: (1) a

---

verification of our algorithm to demonstrate that we retrieve the up- and downgoing virtual Green's functions (using a 1D example for simplicity), (2) a complicated 1D example illustrating our algorithm accurately retrieves the Green's function with and without the free-surface multiples, and (3) a 2D numerical example of the virtual Green's function constructed in such a way that we create a wavefield with all the reflections and direct waves from a virtual source. This last numerical example has the discontinuities in the density and the velocity at different locations. We then demonstrate how to apply these retrieved virtual Green's functions for imaging.

## THEORY

To retrieve the Green's function from a virtual receiver in the subsurface for sources on the surface, one solves the Marchenko equations. The retrieval only requires the reflection response at the surface and an estimate of the first-arrival traveltime from the virtual receiver to the surface. The retrieved Green's function can either include free-surface multiples (Singh et al., 2015, 2016) or exclude these multiples (Broggini and Snieder, 2012; Broggini et al., 2012; Wapenaar et al., 2013, 2014; Slob et al., 2014).

In addition to the retrieved Green's function, the Marchenko equations also give us the one-way focusing functions. These functions are outputs from the Marchenko equations that exist at the acquisition level $\partial D_0$ (the acquisition surface) and focus on an arbitrary depth level $\partial D_i$ at $t = 0$ (the time is equal to zero).

The focusing functions are auxiliary wavefields that reside in a truncated medium that has the same material properties as the actual inhomogeneous medium between $\partial D_0$ and $\partial D_i$ and that is homogeneous above $\partial D_0$ and reflection-free below $\partial D_i$ (Slob et al., 2014). Therefore, the boundary conditions on $\partial D_0$ and $\partial D_i$ in the truncated medium, in which the focusing function exists, are reflection free (see Figure 1). Our algorithm moves the sources of the Green's function retrieved by the Marchenko equations from the surface into the subsurface at a virtual point with the help of the focusing function.

In this paper, the spatial coordinates are defined by their horizontal and depth components; for instance, $\mathbf{x_0} = (\mathbf{x_H}, x_{3,0})$, where $\mathbf{x_H}$ stands for the horizontal coordinates at a depth $x_3$ at the datum $\partial D_0$,
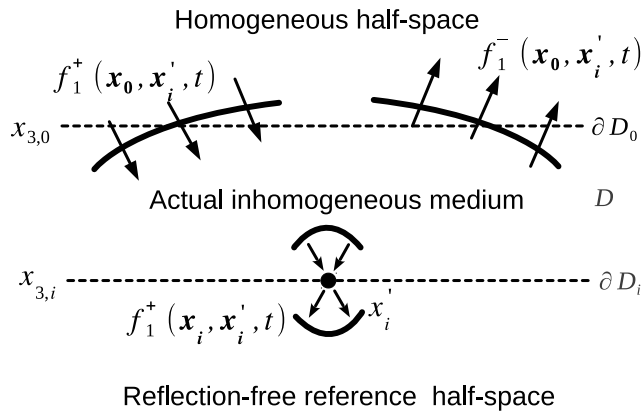
whereas $\mathbf{x_i} = (\mathbf{x_H}, x_{3,i})$ at the datum $\partial D_i$. Superscript $(+)$ refers to downgoing waves and $(-)$ refers to upgoing waves at the observation point $\mathbf{x}$. For Green's functions labeled as $G^{\pm}$, the superscript refers either to downgoing waves $(+)$ or to upgoing waves $(-)$ at the observation point $\mathbf{x}$. In addition, wavefield quantity with a subscript zero (e.g., $R_0$) indicates that no free surface is present.

One-way reciprocity theorems of the convolution and correlation type (equations 1 and 2) are used to relate up- and downgoing fields at arbitrary depth levels to each other in different wave states (Wapenaar and Grimbergen, 1996). The one-way reciprocity theorems (for pressure-normalized wavefields) of the convolution and correlation type are

$$\int_{\partial D_0} \rho^{-1}(\mathbf{x})[(p_A^+)\partial_3 p_B^- + p_A^-(\partial_3 p_B^+)]d\mathbf{x_0} =$$
$$-\int_{\partial D_i} \rho^{-1}(\mathbf{x})[(\partial_3 p_A^+)p_B^- + (\partial_3 p_A^-)p_B^+]d\mathbf{x_i}, \quad (1)$$

$$\int_{\partial D_0} \rho^{-1}(\mathbf{x})[(p_A^+)^*(\partial_3 p_B^+) + (p_A^-)^*(\partial_3 p_B^-)]d\mathbf{x_0} =$$
$$-\int_{\partial D_i} \rho^{-1}(\mathbf{x})[(\partial_3 p_A^+)^* p_B^+ + (\partial_3 p_A^-)^* p_B^-]d\mathbf{x_i}, \quad (2)$$

where the asterisk * denotes complex conjugation; subscripts $A$ and $B$ are two wave states, where $p_A^{\pm}$ and $p_B^{\pm}$ are the arbitrary solutions of the homogeneous wave equations in the region between the two boundaries; and $\partial D_0$ and $\partial D_i$ are the arbitrary depth levels. To apply equations 1 and 2, we assume that there are no sources between $\partial D_0$ and $\partial D_i$.

The correlation reciprocity theorem (equation 2) is based on time-reversal invariance of our wavefields, which implicitly assumes that the medium is lossless. Also, equation 2 ignores evanescent waves; hence, all our results obtained from equation 2 are spatially band limited (Wapenaar et al., 2004). More details on one-way reciprocity can be obtained in Wapenaar (1998) and Wapenaar et al. (2001, 2004).

Wave state $A$ is defined for the truncated medium, and $p_A$ is the focusing function. The one-way wavefields for wave state $A$ for a source at $\mathbf{x_i'}$ are provided in Table 1 and Figure 1.

The Green's functions in the actual medium are defined as wave state $B$. Although we consider wave states $A$ and $B$ to be the focusing function and Green's function, respectively, these wave states can be interchanged. The one-way wavefields for wave state $B$, the actual medium, for a source at $\mathbf{x_j''}$ are provided in Table 1 and Figure 2. These Green's functions are retrieved using the Marchenko equations and include the primary, internal, and free-surface multiple reflections of the actual medium (Singh et al., 2015, 2016).

We substitute the one-way wavefields described in Table 1 into equations 1 and 2, and we also use the sifting property of the delta function to yield

$$G^-(\mathbf{x_i'}, \mathbf{x_j''}, \omega) = \frac{2}{j\omega} \int_{-\infty}^{\infty} \rho(\mathbf{x_0})^{-1}[\partial_3 G^-(\mathbf{x_0}, \mathbf{x_j''}, \omega)$$
$$\times f_1^+(\mathbf{x_0}, \mathbf{x_i'}, \omega) + r\partial_3 G^-(\mathbf{x_0}, \mathbf{x_j''}, \omega)f_1^-(\mathbf{x_0}, \mathbf{x_i'}, \omega)]d\mathbf{x_0}, \quad (3)$$



Figure 1. Up- and downgoing focusing functions $f_1^{\pm}$ that focus at $\mathbf{x_i'}$ in the truncated medium. This medium is homogeneous above $\partial D_0$ and below $\partial D_i$, and it is equal to the real medium between $\partial D_0$ and $\partial D_i$.

$$G^+(\mathbf{x}'_i,\mathbf{x}''_j,\omega)=-\frac{2}{j\omega}\int_{-\infty}^{\infty}\rho(\mathbf{x_0})^{-1}[r\partial_3 G^-(\mathbf{x_0},\mathbf{x}''_j,\omega)$$
$$\times f_1^+(\mathbf{x_0},\mathbf{x}'_i,\omega)^*+\partial_3 G^-(\mathbf{x_0},\mathbf{x}''_j,\omega)f_1^-(\mathbf{x_0},\mathbf{x}'_i,\omega)^*]d\mathbf{x_0}, \qquad (4)$$

where $r$ denotes the reflection coefficient of the free surface (in the examples shown in this paper, $r=-1$). Note that equations 3 and 4 yield the up- and downgoing virtual Green's functions, respectively, for a virtual receiver at $\mathbf{x}'_i$ above a virtual source at $\mathbf{x}''_j$ in the subsurface; i.e., $x_{3,i} < x_{3,j}$.

In equations 3 and 4, we interchange $\mathbf{x}'_i$ and $\mathbf{x}''_j$ leading to

$$G^-(\mathbf{x}''_j,\mathbf{x}'_i,\omega)=\frac{2}{j\omega}\int_{-\infty}^{\infty}\rho(\mathbf{x_0})^{-1}[\partial_3 G^-(\mathbf{x_0},\mathbf{x}'_i,\omega)$$
$$\times f_1^+(\mathbf{x_0},\mathbf{x}''_j,\omega)+r\partial_3 G^-(\mathbf{x_0},\mathbf{x}'_i,\omega)f_1^-(\mathbf{x_0},\mathbf{x}''_j,\omega)]d\mathbf{x_0}, \qquad (5)$$

$$G^+(\mathbf{x}''_j,\mathbf{x}'_i,\omega)=-\frac{2}{j\omega}\int_{-\infty}^{\infty}\rho(\mathbf{x_0})^{-1}[r\partial_3 G^-(\mathbf{x_0},\mathbf{x}'_i,\omega)$$
$$\times f_1^+(\mathbf{x_0},\mathbf{x}''_j,\omega)^*+\partial_3 G^-(\mathbf{x_0},\mathbf{x}'_i,\omega)f_1^-(\mathbf{x_0},\mathbf{x}''_j,\omega)^*]d\mathbf{x_0}. \qquad (6)$$

The retrieved one-way Green's functions in equations 5 and 6 are for a virtual receiver $\mathbf{x}''_j$ above the virtual source $\mathbf{x}'_i$. We add equation 3 to equation 4 and equation 5 to equation 6, yielding

$$G(\mathbf{x}'_i,\mathbf{x}''_j,\omega)=\frac{2}{j\omega}\int_{-\infty}^{\infty}\rho(\mathbf{x_0})^{-1}[\partial_3 G^-(\mathbf{x_0},\mathbf{x}''_j,\omega)$$
$$\times f_2(\mathbf{x}'_i,\mathbf{x_0},\omega)+r\partial_3 G^-(\mathbf{x_0},\mathbf{x}''_j,\omega)f_2(\mathbf{x}'_i,\mathbf{x_0},\omega)^*]d\mathbf{x_0}, \qquad (7)$$

$$G(\mathbf{x}''_j,\mathbf{x}'_i,\omega)=\frac{2}{j\omega}\int_{-\infty}^{\infty}\rho(\mathbf{x_0})^{-1}[\partial_3 G^-(\mathbf{x_0},\mathbf{x}'_i,\omega)$$
$$\times f_2(\mathbf{x}''_j,\mathbf{x_0},\omega)+r\partial_3 G^-(\mathbf{x_0},\mathbf{x}'_i,\omega)f_2(\mathbf{x}''_j,\mathbf{x_0},\omega)^*]d\mathbf{x_0}, \qquad (8)$$

where $f_2(\mathbf{x}'_i,\mathbf{x_0},\omega)=f_1^+(\mathbf{x_0},\mathbf{x}'_i,\omega)-f_1^-(\mathbf{x_0},\mathbf{x}'_i,\omega)^*$ (Singh et al., 2015).

Applying the source-receiver reciprocity to equation 8, we obtain

$$G(\mathbf{x}'_i,\mathbf{x}''_j,\omega)=\frac{2}{j\omega}\int_{-\infty}^{\infty}\rho(\mathbf{x_0})^{-1}[\partial_3 G^-(\mathbf{x_0},\mathbf{x}'_i,\omega)$$
$$\times f_2(\mathbf{x}''_j,\mathbf{x_0},\omega)+r\partial_3 G^-(\mathbf{x_0},\mathbf{x}'_i,\omega)f_2(\mathbf{x}''_j,\mathbf{x_0},\omega)^*]d\mathbf{x_0}. \qquad (9)$$

Equation 9 yields Green's function for a virtual reciever below a virtual source. By adding equations 7–9, we yield the virtual Green's function, at an arbitrary receiver $\mathbf{x}'_i$ for an arbitrary source at $\mathbf{x}''_j$:

$$G(\mathbf{x}'_i,\mathbf{x}''_j,\omega)=\frac{2}{j\omega}H(x''_{3,j}-x'_{3,i})\int_{-\infty}^{\infty}\rho(\mathbf{x_0})^{-1}[\partial_3 G^-(\mathbf{x_0},\mathbf{x}''_j,\omega)$$
$$\times f_2(\mathbf{x}'_i,\mathbf{x_0},\omega)+r\partial_3 G^-(\mathbf{x_0},\mathbf{x}''_j,\omega)f_2(\mathbf{x}'_i,\mathbf{x_0},\omega)^*]d\mathbf{x_0}+$$
$$\frac{2}{j\omega}H(x'_{3,i}-x''_{3,j})\int_{-\infty}^{\infty}\rho(\mathbf{x_0})^{-1}[\partial_3 G^-(\mathbf{x_0},\mathbf{x}'_i,\omega)$$
$$\times f_2(\mathbf{x}''_j,\mathbf{x_0},\omega)+r\partial_3 G^-(\mathbf{x_0},\mathbf{x}'_i,\omega)f_2(\mathbf{x}''_j,\mathbf{x_0},\omega)^*]d\mathbf{x_0}. \qquad (10)$$

We include the Heaviside functions to indicate that the virtual receiver $x'_{3,i}$ is either above $\{H(x''_{3,j}-x'_{3,i})\}$ or below $\{H(x'_{3,i}-x''_{3,j})\}$ the virtual source $x''_{3,j}$.

Note that the retrieved virtual Green's functions in equation 10 are not limited to the source $\mathbf{x}''_j$ being below the receiver $\mathbf{x}'_i$, but they hold for arbitrary positions in the subsurface of the virtual receivers $\mathbf{x}'_i$ and virtual sources $\mathbf{x}''_j$.

To compute the virtual Green's function in equation 10, we require (1) Green's function $G^-(\mathbf{x_0},\mathbf{x},\omega)$ at the surface $\mathbf{x_0}$ for a virtual source at $\mathbf{x}'_i$ and $\mathbf{x}''_j$ and (2) the focusing function $f^\pm(\mathbf{x_0},\mathbf{x},\omega)$ at the surface $\mathbf{x_0}$ for a focal point at $\mathbf{x}'_i$ and $\mathbf{x}''_j$. We retrieve both functions by solving the Marchenko equations using only the reflection response (including free-surface multiples) at the surface and a smooth version of the velocity.

We can also retrieve the virtual Green's function that does not include free-surface multiples by setting the reflection coefficient $r$ at the free surface to zero in equation 10. Thus, the equation to retrieve the virtual Green's function without the presence of a free surface is

**Table 1. The wavefields of the focusing function $f_1$ and Green's functions at the acquisition surface $\partial D_0$ and the level $\partial D_i$. The term $p_A^\pm$ symbolizes the one-way wavefields in the frequency domain for wave state $A$, at arbitrary depth levels in the reference medium (see Figure 1), whereas $p_B^\pm$ symbolizes one-way wavefields at arbitrary depth levels in the inhomogeneous medium in wave state $B$, where $r$ is the reflection coefficient of the free surface (see Figure 2).**

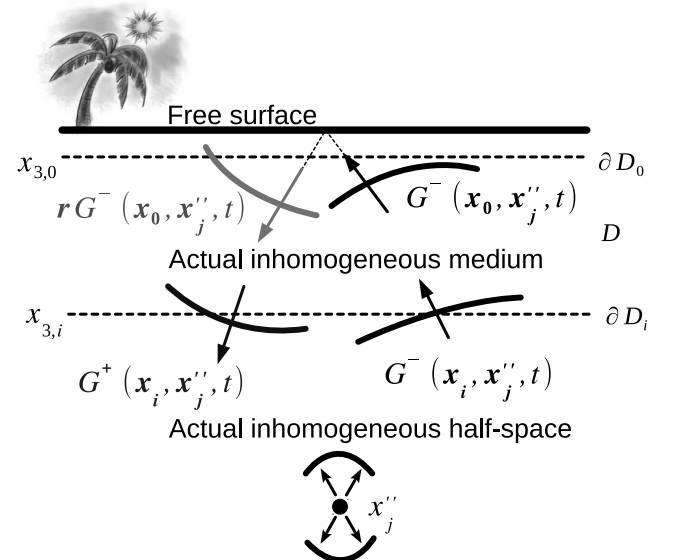|  | State $A$ | State $B$ |
|---|---|---|
| On $\partial D_0$ | $p_A^+ = f_1^+(\mathbf{x_0},\mathbf{x}'_i,\omega)$ | $\partial_3 p_B^+ = r\partial_3 G^-(\mathbf{x_0},\mathbf{x}''_j,\omega)$ |
|  | $p_A^- = f_1^-(\mathbf{x_0},\mathbf{x}'_i,\omega)$ | $\partial_3 p_B^- = \partial_3 G^-(\mathbf{x_0},\mathbf{x}''_j,\omega)$ |
| On $\partial D_i$ | $\partial_3 p_A^+ = \partial_3 f_1^+(\mathbf{x_i},\mathbf{x}'_i,\omega) = -\frac{1}{2}j\omega\rho(\mathbf{x}'_i)\delta(\mathbf{x}_H - \mathbf{x}'_H)$ | $p_B^+ = G^+(\mathbf{x_i},\mathbf{x}''_j,\omega)$ |
|  | $\partial_3 p_A^- = \partial_3 f_1^-(\mathbf{x_i},\mathbf{x}'_i,\omega) = 0$ | $p_B^- = G^-(\mathbf{x_i},\mathbf{x}''_j,\omega)$ |



Figure 2. The Green's functions in the actual inhomogeneous medium in the presence of a free surface at the acquisition surface $\partial D_0$ and the arbitrary surface $\partial D_i$. The tree indicates the presence of the free surface.

$$G_0(\mathbf{x}_i', \mathbf{x}_j'', \omega) = \frac{2}{j\omega} H(x_{3,j}'' - x_{3,i}') \int_{-\infty}^{\infty} \rho(\mathbf{x_0})^{-1} [\partial_3 G_0^-(\mathbf{x_0}, \mathbf{x}_j'', \omega)$$

$$\times f_2(\mathbf{x}_i', \mathbf{x_0}, \omega)] d\mathbf{x_0} +$$

$$\frac{2}{j\omega} H(x_{3,i}' - x_{3,j}'') \int_{-\infty}^{\infty} \rho(\mathbf{x_0})^{-1} [\partial_3 G_0^-(\mathbf{x_0}, \mathbf{x}_i', \omega) f_2(\mathbf{x}_j'', \mathbf{x_0}, \omega)] d\mathbf{x_0},$$

$$(11)$$

where $G_0(\mathbf{x}_i', \mathbf{x}_j'', \omega)$ is the virtual Green's function without free-surface multiples for a virtual receiver at $\mathbf{x}_i'$ and virtual source at $\mathbf{x}_j''$.

## NUMERICAL EXAMPLES

To show a proof of concept for our algorithm, we begin with a simple 1D numerical example. Our model consists of two homogeneous layers separated by an interface at 0.5 km with constant density and velocity in each layer and a free surface. At the interface, the velocity changes from 2 to 2.8 km, whereas the density changes from 1 to 2.5 g cm$^{-3}$.
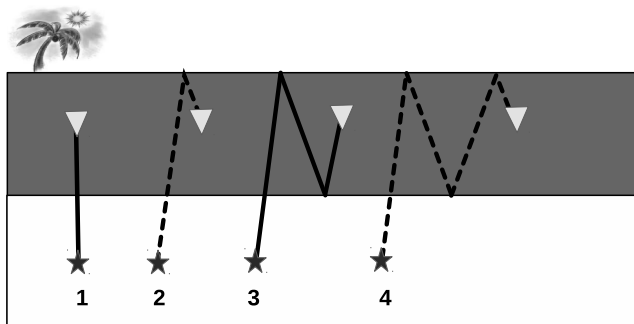


Figure 3. Schematic of the up- and downgoing events at the receiver position for the simple two-layer model. The solid lines represent upgoing events, whereas dotted events represent downgoing events.
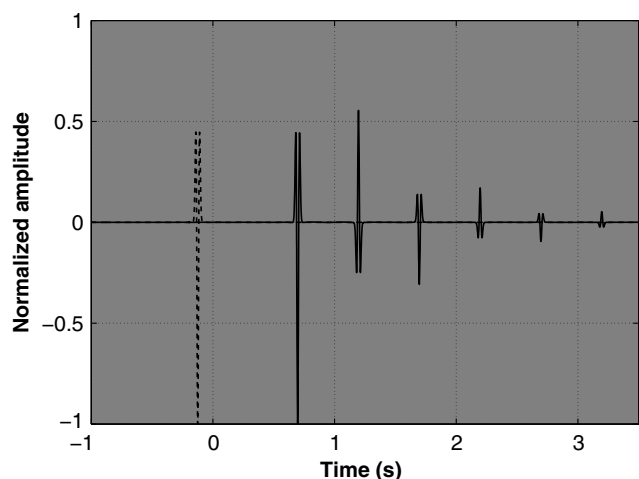


Figure 4. The input wavefields required for equations 3 and 4. The two-way Green's functions $G(\mathbf{x_0}, \mathbf{x}_j'', t)$ (solid line) retrieved by the Marchenko equations in the presence of a free surface for $\mathbf{x}_j'' = 1.75$ km and the downgoing focusing function $f^+(\mathbf{x_0}, \mathbf{x}_i', t)$ (dotted line) solved by the Marchenko equations for $\mathbf{x}_i' = 0.25$ km.

Our objective is to retrieve the virtual up- and downgoing Green's functions $G^\pm(\mathbf{x}_i', \mathbf{x}_j'', \omega)$ at the virtual receiver $\mathbf{x}_i' = 0.25$ km for a virtual source at $\mathbf{x}_j'' = 1.75$ km; a schematic of these waves is shown in Figure 3. To retrieve the virtual Green's function, we solve equations 3 and 4. These equations require at the surface $\mathbf{x_0}$: (1) The focusing function $f_1^\pm(\mathbf{x_0}, \mathbf{x}_i', t)$ and (2) Green's function $G(\mathbf{x_0}, \mathbf{x}_j'', t)$ with their virtual source locations at $\mathbf{x}_i'$ and $\mathbf{x}_j''$, respectively. The focusing functions are up- and downgoing at the surface $\partial D_0$, and they are shaped to focus at the virtual receiver $\mathbf{x}_i' = 0.25$ km for $t = 0$.

We retrieve the one-way focusing functions at the surface by solving the Marchenko equations (Singh et al., 2015, 2016). The downgoing focusing function is shown in Figure 4 by the dotted line (normalized by its maximum amplitude). Because the medium between the surface and the focusing point is homogeneous, the upgoing focusing function vanishes because it suffices to only have a downgoing focusing function to create a focus at $\mathbf{x}_i' = 0.25$ km (see Figure 4).

The Green's function $G^-(\mathbf{x_0}, \mathbf{x}_j'', t)$ (on the right side of equations 3 and 4) needed for our virtual Green's function (on the left side of equations 3 and 4) is retrieved by the Marchenko equations as well. The function $G^-(\mathbf{x_0}, \mathbf{x}_j'', t)$ includes free-surface multiples, internal multiples, and primaries. The function $G^-(\mathbf{x_0}, \mathbf{x}_j'', t)$ is the response of a virtual source at $\mathbf{x}_j'' = 1.75$ km recorded at the surface $\partial D_0$ (see Figure 4).

To solve the Marchenko equation, to obtain the focusing functions $f^\pm(\mathbf{x_0}, \mathbf{x}_i', t)$ and the Green's function $G^-(\mathbf{x_0}, \mathbf{x}_j'', t)$ and, consequently, the virtual Green's function from equations 3 and 4, we require the reflection response at the acquisition level (which includes all multiples and primaries) and an estimate of the traveltime from each of the virtual points to the acquisition level.

By substituting $G^-(\mathbf{x_0}, \mathbf{x}_j'', t)$ and $f^\pm(\mathbf{x_0}, \mathbf{x}_i', t)$ (shown in Figure 4) into equations 3 and 4 and adding the corresponding up- and downgoing virtual Green's functions, we obtain the two-way virtual Green's function $G(\mathbf{x}_i', \mathbf{x}_j'', t)$ recorded at a virtual receiver
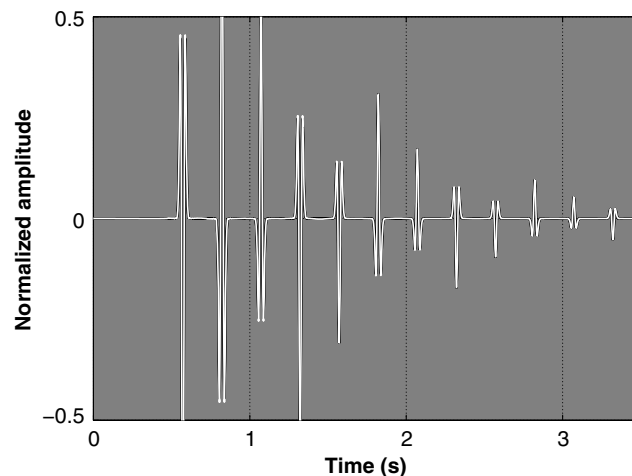


Figure 5. Green's function with virtual source $\mathbf{x}_j''$ at depth 1.75 km and recording at the virtual receiver $\mathbf{x}_i'$ at depth 0.25 km. The thicker black line is the modeled Green's function, and superimposed on it is the retrieved Green's function. Each trace is divided by its maximum amplitude; hence, the y-axis label is called normalized amplitude. The plot limits are chosen between 0.5 and −0.5 normalized amplitude to visualize the smaller amplitude events better.

located at $\mathbf{x}_i' = 0.25$ km and a virtual source located at $\mathbf{x}_j'' = 1.75$ km (see Figure 5). This figure illustrates that we can accurately retrieve the virtual Green's function because there is minimal mismatch with the modeled Green's function (in black; the source is at 1.75 km, and the receiver is at 0.25 km). The modeled Green's function is computed using finite difference with the exact velocity and density. Note that the plots that compare the virtual Green's function with the modeled Green's functions are normalized because we do not retrieve the virtual Green's function with the correct amplitudes but with the correct relative amplitudes.

Figure 3 shows a schematic of a few of the up- (solid lines) and downgoing (dashed lines) events at the virtual receiver above the virtual source in our one-interface model. These events (numbered) in Figure 3 correspond to the retrieved virtual up- and downgoing Green's functions in Figure 6, at the correct traveltimes, hence, confirming the proof of concept of our one-way equations in equations 3 and 4.
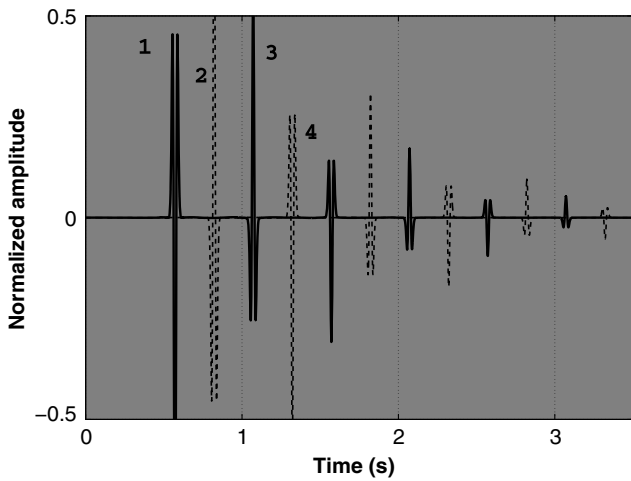


Figure 6. The up- (solid line) and the downgoing (dotted line) Green's functions with the numbers in Figure 3 corresponding to the the appropriate event.
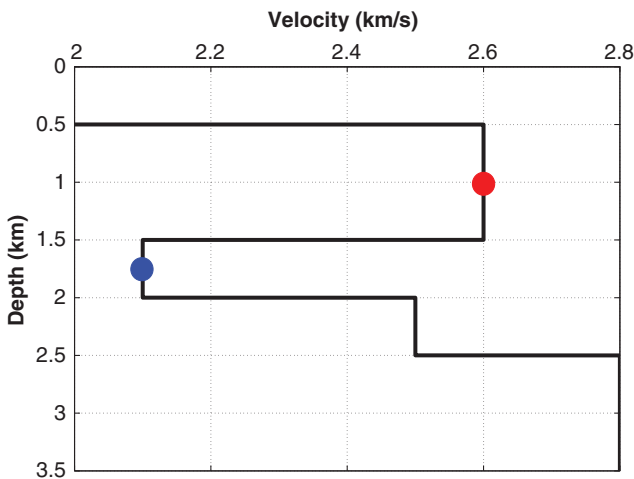


Figure 7. The 1D velocity model without a free surface. The red dot at 0.75 km is the location of the virtual receiver, whereas the blue dot at 1.75 km is the position of the virtual source for the retrieved virtual Green's function.

The second example illustrates the retrieval of the virtual Green's function without the free-surface reflections for the model given in Figure 7 with the virtual source and receiver shown by the red and blue dots, respectively. This example also contains variable density, with discontinuities at the same depth as the velocity model, with densities ranging from 1 to 3 g cm$^{-3}$. As shown in Figure 8 (the virtual Green's function in the second example), there is an almost perfect match between the modeled Green's function and the retrieved virtual Green's function.

Figure 9 shows the virtual Green's function using the same model in Figure 7 but with free-surface multiples. We note the increased reflections and complexity that the free surface introduces (Figure 9) compared to the case without the free surface (Figure 8). The match between the modeled Green's function and the retrieved Green's function using our algorithm is almost exact (see Figure 9).
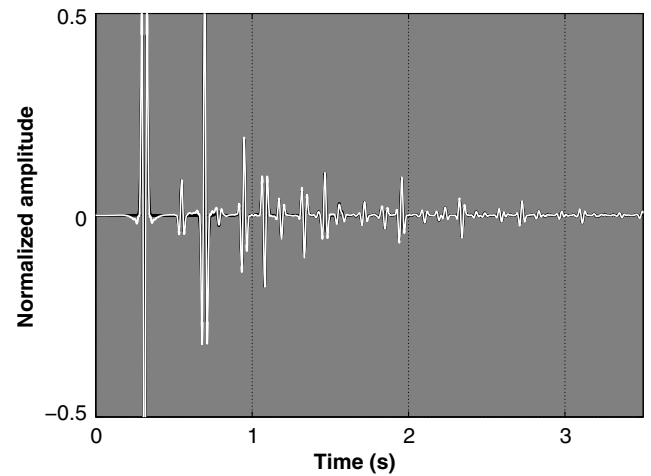


Figure 8. Virtual Green's function (white line) with virtual source $\mathbf{x}_j''$ at depth 1.75 km and recording at the virtual receiver $\mathbf{x}_i'$ at depth 0.75 km superimposed on it the modeled Green's function (black line). Both Green's functions do not include free-surface multiples.
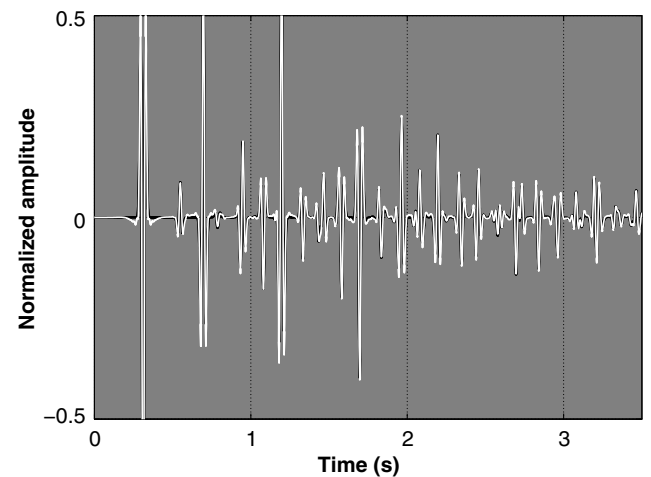


Figure 9. Virtual Green's function with free-surface multiples (white line) with virtual source $\mathbf{x}_j''$ at depth 1.75 km and recording at the virtual receiver $\mathbf{x}_i'$ at depth 0.75 km for the model in Figure 7 with a free surface. The modeled Green's function is superimposed on it, which also includes the free-surface multiples (black line).

The 1D numerical examples have perfect aperture; hence, the 1D examples almost perfectly match the retrieved virtual Green's function to the modeled Green's function. The equations to obtain the virtual Green's function are multidimensional. We next show a 2D numerical example of the virtual Green's function in a velocity and density model shown in Figures 10 and 11, respectively. Notice that the discontinuities and the dip of the interfaces in the velocity are different from those in the density.

Our algorithm allows us to place virtual receivers and virtual sources in any target location in the subsurface. For our numerical example, we retrieve the virtual Green's function $G(\mathbf{x}_i', \mathbf{x}_j'', t)$ (Figure 12), where $\mathbf{x}_i'$ are the virtual receivers populating the target location at every 32 m (black box in Figure 10) and $\mathbf{x}_j'' = (0, 0.7)$ km is the virtual source (black dot in Figure 10). In Figure 12, we notice that

1) In Figure 12b, the first arrival from the virtual source $\mathbf{x}_j'' = (0, 0.7)$ km and the reflection from the bottom velocity layer.
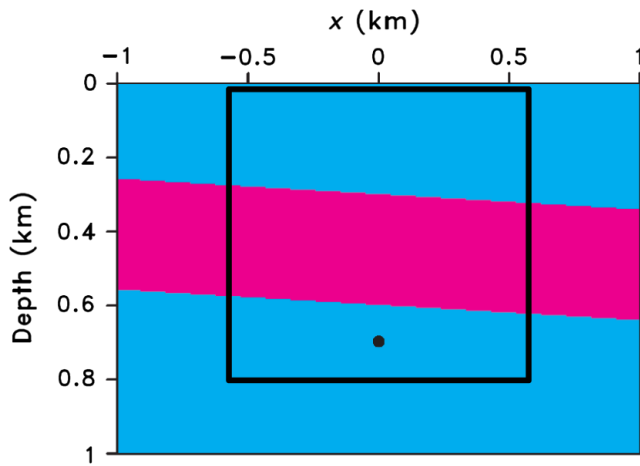


Figure 10. Two-interface velocity model with velocities ranging from 2.0 to 2.4 km/s. The dot shows the position of the virtual source for the virtual Green's function, and the black box is the target zone in which we place virtual receivers.
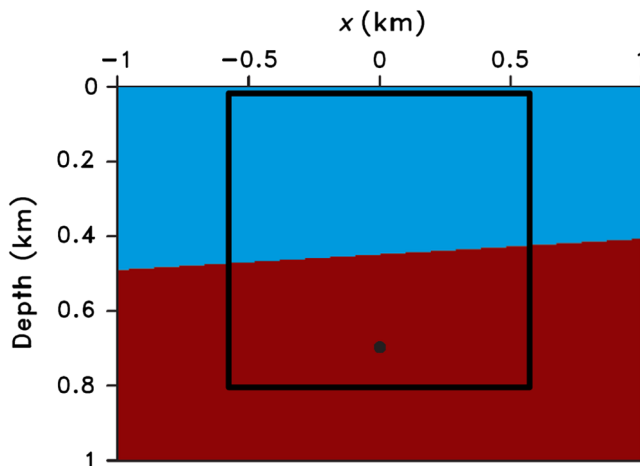


Figure 11. One-interface density model with densities ranging from 2.0 to 3.0 g cm³. The dot shows the position of the virtual source for the virtual Green's function, and the black box is the target zone in which we place virtual receivers.

2) In Figure 12c and 12d, the inability of our algorithm to handle the horizontal propagating energy of the first arrival from the virtual source, hence, the dimming on the sides of the first arrival of the virtual Green's function. To retrieve near-horizontally propagating events (in this case, these waves are not evanescent) especially in the first arrival of the virtual Green's function, we also require a much larger aperture than is used in this example. Note that the later arriving up- and downward propagating waves are retrieved accurately at the depth of the virtual source $\mathbf{x}_j'' = (0, 0.7)$ km in Figure 12d and 12e because the reflections are purely up- and downgoing.

3) In Figure 12c and 12d, we do, however, retrieve the reflections from the density layer (the pink line in Figure 12), although we did not use any information of the density model in our numerical retrieval of the virtual Green's function.

4) In Figure 12f, the free-surface multiple is present. As expected, there is a polarity change of the free-surface multiple compared with the incident wave at the top of Figure 12e due to the interaction of this wave in Figure 12e with the free surface.

5) In Figure 12h, we obtain the upgoing reflections caused by the free-surface multiple interacting with the velocity and density layer.

We compare in Figure 13, a trace of the virtual Green's function $G(\mathbf{x}_i', \mathbf{x}_j'', t)$ at virtual location $\mathbf{x}_i' = (0, 0.17)$ km and $\mathbf{x}_j'' = (0, 0.7)$ km to the modeled Green's function, with physical receiver and physical source at the virtual receiver and virtual source location $\mathbf{x}_i'$ and $\mathbf{x}_j''$, respectively. The modeled Green's function in Figure 13 is generated by finite differences using the exact velocity and density. The trace of the virtual Green's function is comparable with the modeled Green's function, as shown in Figure 13.

In our algorithm, we evaluate an integral over space using a sampling interval $dx$, for example, in equations 3 and 4. These integrals over space, which include the stationary phase contribution, also generate artifacts due to end-point contributions. Similar to interferometry, these artifacts can be mitigated through tapering at the edges of the integration interval (Mehta et al., 2008; van der Neut and Thorbecke, 2009). In our 2D model, these artifacts that arise from the integrals over space are also present. We remove these artifacts by muting the wavefield before the first arrival of the virtual source $\mathbf{x}_j''$, and estimate the traveltime of the first arrival using the smooth velocity model.

We use the up- and downgoing Green's functions to image the subsurface (see Figure 14) similar to the work of Wapenaar et al. (2014) and Singh et al. (2015, 2016). The inputs to construct this image are only a smooth version of the velocity in Figure 10 and the reflection response (including the free-surface multiples) at the surface. Note that the reflection response is the deconvolution of the reflected waves data at the surface with the wavelet; hence, the wavelet is assumed to be known. In our imaging example (Figure 14), we correlate the up- and downgoing virtual Green's functions at each virtual receiver location evaluated at zero time for a virtual source at $\mathbf{x}_j'' = (0, 0.7)$ km. We can apply other imaging conditions to the up- and downgoing virtual Green's functions, as described in Singh and Snieder (2016) that reduces the artifacts caused by multiples.

Note that we are imaging with the source located below the reflectors (at $\mathbf{x}_j'' = (0, 0.7)$ km) which is different from other methods that use the Marchenko equations for imaging (Marchenko imaging), in which the source must be at the surface. For comparison, we show the conventional Marchenko image, in which sources

are limited to the surface (Figure 15). Note that the polarity for the Marchenko image (Figure 15) is opposite to our method of imaging (Figure 14) because the source is below the reflectors for our method. Note the difference in the bandwidth of the shallowest reflector in Figures 14 and 15. This difference is caused by a difference in the vertical wavenumbers that sample the reflector (Bleistein et al., 2013).

We also constructed Green's functions and the associated image with an incorrect velocity model, as shown in Figure 16 with the virtual source at the same depth, as shown in Figure 14 at $\mathbf{x}_j'' = (0, 0.7)$ km. This velocity model is a homogeneous model with the velocity of the first layer in Figure 10, hence, the correct positioning of the first layer. Note that although the velocity model is incorrect, we do not get spurious reflectors from the mishandling

of the multiples. The image constructed with a smooth version of the velocity model in Figure 14 (no small-scale details of the velocity model are included) differs from the image constructed with the wrong velocity in Figure 16, only in the positions of the interfaces.

## DISCUSSION

A fair question to ask is: Why not use interferometry to cross-correlate the Green's function at a virtual receiver and at a virtual source to get the virtual Green's function between the virtual source and the receiver? This interferometric method will not retrieve the virtual Green's function because we do not have a closed surface of sources, which is required by seismic interferometry. In Figure 17 (the red line), we show the interferometric Green's function (the
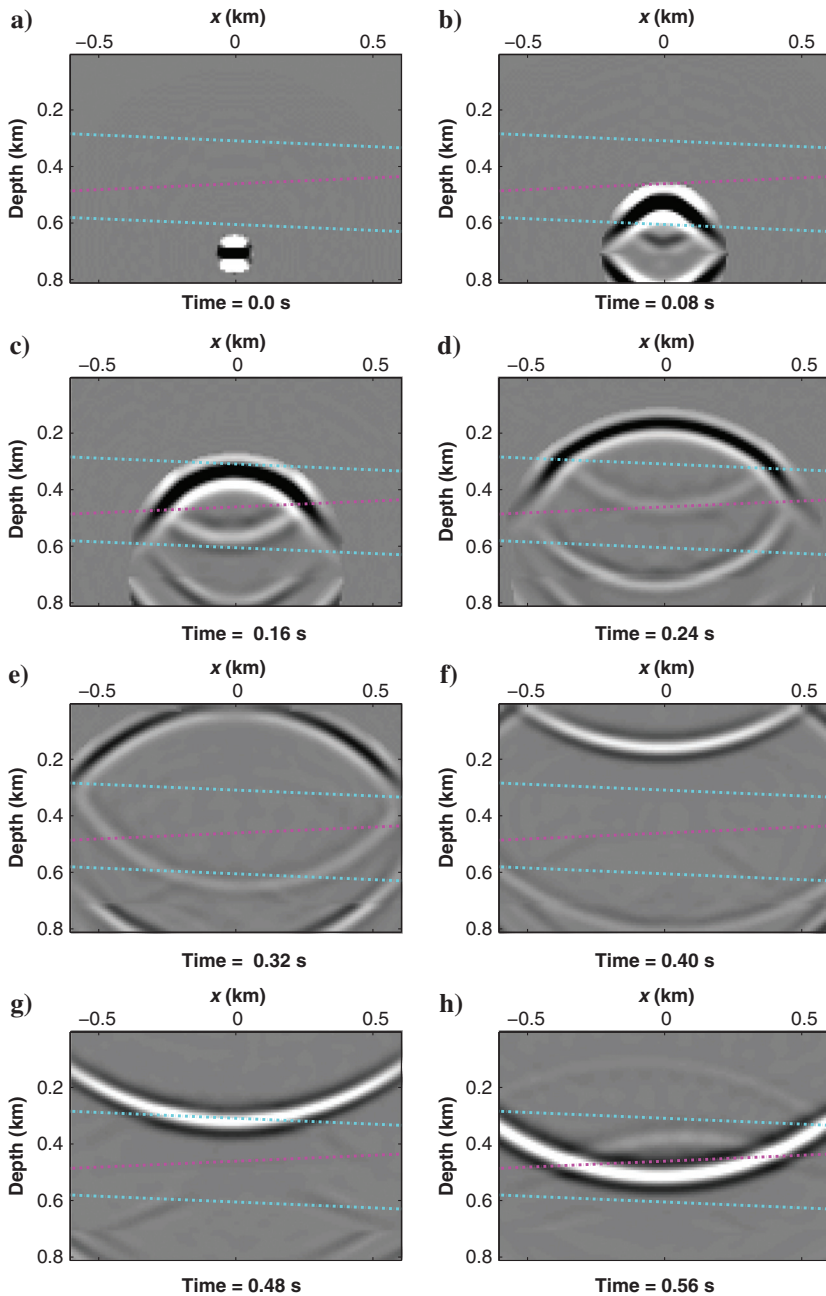


Figure 12. Snapshots of the virtual Green's function $G(\mathbf{x}_i', \mathbf{x}_j'', t)$ with virtual sources $\mathbf{x}_j'' = (0, 0.7)$ km and virtual receivers $\mathbf{x}_i'$ populating the target box in Figure 10.
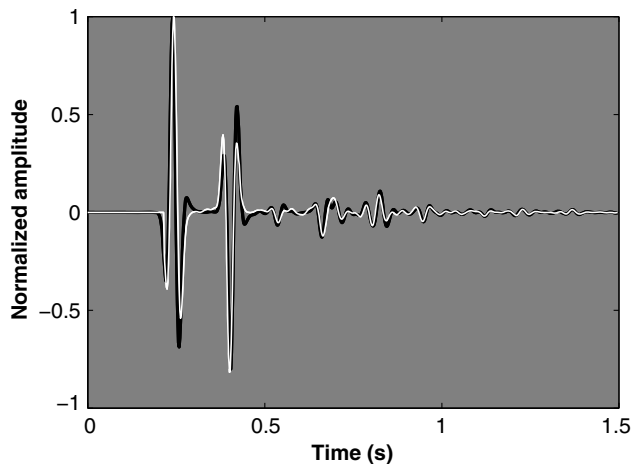
Figure 13. Virtual Green's function (white line) with virtual source $\mathbf{x}_j'' = (0, 0.7)$ km and recording at the virtual receiver $\mathbf{x}_j' = (0, 0.17)$ km for the 2D model in Figure 10. The thicker black line is the modeled Green's function, and the superimposed on it is the retrieved Green's function.
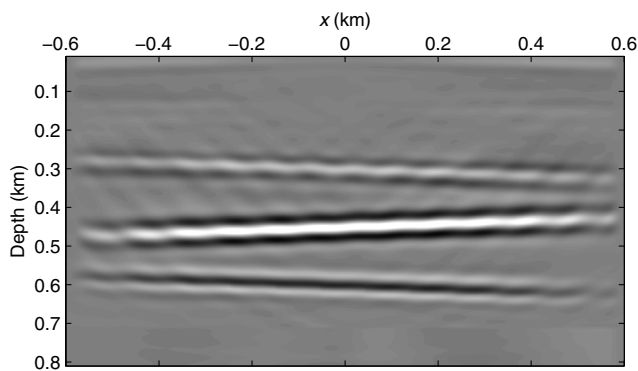


Figure 14. Image of the model in Figures 10 and 11. The imaging condition we use is the correlation of the up- and downgoing Green's functions at each virtual receiver location evaluated at zero time for a virtual source at $\mathbf{x}_j'' = (0, 0.7)$ km. The inputs are a smooth version of the velocity and the reflection response at the surface (includes free-surface multiples).
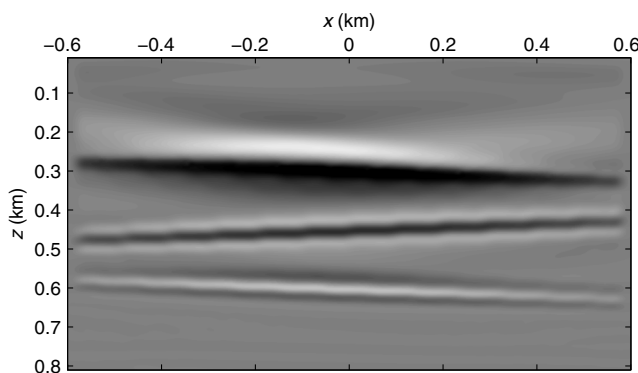


Figure 15. Image of the model in Figures 10 and 11 using the conventional Marchenko imaging with the correlation imaging condition (Broggini et al., 2014; Singh, 2016).

crosscorrelation of the Green's functions from the virtual source and receiver to the surface) for the same model (see Figure 8) with the same virtual source $\mathbf{x}_j'' = 1.75$ km and virtual receiver $\mathbf{x}_i' = 0.25$ km locations in the second 1D example.

Because we have reflectors below the virtual source location $\mathbf{x}_j'' = 1.75$ km (see Figure 7), our physical sources are at the surface, and we include a free surface, our interferometric Green's function does not match the modeled or virtual Green's function (see Figure 17, the white line).

For the simple 2D model, the discontinuities and dip in the velocity and density are different. However, we retrieve the two- and one-way wavefields of the virtual Green's function without any knowledge of the density model or the position and strengths of the interfaces. Figure 12 shows reflections from the density interface (middle interface in Figure 12), even though no density information was included in
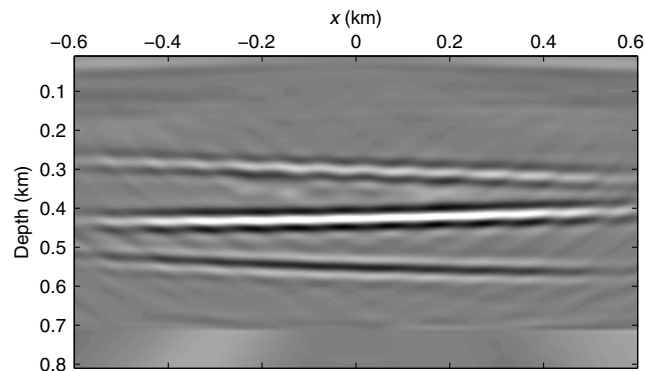


Figure 16. Image of the model in Figures 10 and 11. The imaging condition we use is the correlation of the up- and downgoing Green's functions at each virtual receiver location evaluated at zero time and zero offset. The inputs are a constant velocity (kinematics are incorrect compared with the actual velocity model in Figure 10) and the reflection response at the surface (includes free-surface multiples).
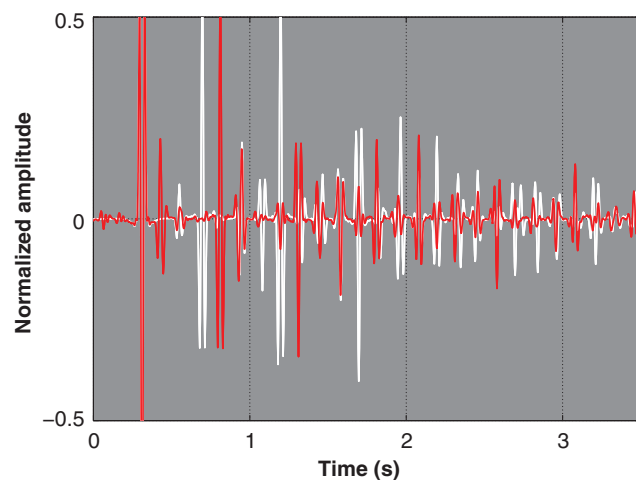


Figure 17. Virtual Green's function with virtual source $\mathbf{x}_j''$ at depth 1.75 km and recording at the virtual receiver $\mathbf{x}_i'$ at depth 0.75 km retrieved by the method of this paper (white line) and computed by interferometry (red line). The retrieved virtual Green's function (white line) is almost identical to the modeled virtual Green's function.

our algorithm. We retrieve these reflections because the density information is embedded in the reflection response recorded at the surface and the Marchenko equations are able to retrieve the density reflections from this response.

In the case in which the kinematics of the first arrivals at the virtual locations to the surface are incorrect (incorrect velocity model), the retrieved virtual Green's functions are incorrect, yet we still avoid the artifacts from the multiples in the associated image.

## CONCLUSION

We can retrieve Green's function between two points in the subsurface with single-sided illumination. In general, interferometry gives inaccurate Green's functions for illumination from above (single-sided) because we do not have the illumination contributions from below. However, the Marchenko equations can be thought of as the mechanism to obviate the need for illumination from below to retrieve the virtual Green's function. The removal of the requirement for illumination from below (for interferometry) comes from the use of the focusing function, a solution to the Marchenko equations. The events in the focusing function only depend on the truncated medium, and this function is solved using illumination only from above. We explore this single-side illumination advantage of the focusing function to avoid the illumination from below to retrieve the virtual Green's function. Our numerical examples demonstrate that we can image the subsurface either above and/or below our target zone.

## ACKNOWLEDGMENTS

## REFERENCES

Bakulin, A., and R. Calvert, 2006, The virtual source method: Theory and case study: Geophysics, **71**, no. 4, SI139–SI150, doi: 10.1190/1.2216190.

Bleistein, N., J. K. Cohen, and J. Stockwell, 2013, Mathematics of multi-dimensional seismic imaging, migration, and inversion: Springer Science & Business Media.

Broggini, F., and R. Snieder, 2012, Connection of scattering principles: A visual and mathematical tour: European Journal of Physics, **33**, 593–613, doi: 10.1088/0143-0807/33/3/593.

Broggini, F., R. Snieder, and K. Wapenaar, 2012, Focusing the wavefield inside an unknown 1D medium: Beyond seismic interferometry: Geophysics, **77**, no. 5, A25–A28, doi: 10.1190/geo2012-0060.1.

Broggini, F., R. Snieder, and K. Wapenaar, 2014, Data-driven wavefield focusing and imaging with multidimensional deconvolution: Numerical ex-amples for reflection data with internal multiples: Geophysics, **79**, no. 3, WA107–WA115, doi: 10.1190/geo2013-0307.1.

Curtis, A., P. Gerstoft, H. Sato, R. Snieder, and K. Wapenaar, 2006, Seismic interferometry: Turning noise into signal: The Leading Edge, **25**, 1082–1092, doi: 10.1190/1.2349814.

Curtis, A., and D. Halliday, 2010, Source-receiver wave field interferometry: Physical Review E, **81**, 046601, doi: 10.1103/PhysRevE.81.046601.

Curtis, A., H. Nicolson, D. Halliday, J. Trampert, and B. Baptie, 2009, Virtual seismometers in the subsurface of the earth from seismic interferometry: Nature Geoscience, **2**, 700–704, doi: 10.1038/ngeo615.

Mehta, K., R. Snieder, R. Calvert, and J. Sheiman, 2008, Acquisition geometry requirements for generating virtual-source data: The Leading Edge, **27**, 620–629, doi: 10.1190/1.2919580.

Singh, S., 2016, An inverse scattering approach to imaging using Marchenko equations in the presence of a free surface: Doctor of Philosophy (Geophysics) thesis, Colorado School of Mines.

Singh, S., and R. Snieder, 2016, Strategies for imaging with Marchenko-retrieved Greens functions: 86th Annual International Meeting, SEG, Expanded Abstracts, 4434–4439.

Singh, S., R. Snieder, J. Behura, J. van der Neut, K. Wapenaar, and E. Slob, 2015, Marchenko imaging: Imaging with primaries, internal multiples, and free-surface multiples: Geophysics, **80**, no. 5, S165–S174, doi: 10.1190/geo2014-0494.1.

Singh, S., R. Snieder, J. Thorbecke, J. van der Neut, K. Wapenaar, and E. Slob, 2016, Incoporating free surface multiples in Marchenko imaging: 85th Annual International Meeting, SEG, Expanded Abstracts, 4328–4333.

Slob, E., K. Wapenaar, F. Broggini, and R. Snieder, 2014, Seismic reflector imaging using internal multiples with Marchenko-type equations: Geophysics, **79**, no. 2, S63–S76, doi: 10.1190/geo2013-0095.1.

Snieder, R., K. Wapenaar, and U. Wegler, 2007, Unified Green's function retrieval by crosscorrelation: Connection with energy principles: Physical Review E, **75**, 036103, doi: 10.1103/PhysRevE.75.036103.

Thorbecke, J. W., and D. Draganov, 2011, Finite-difference modeling experiments for seismic interferometry: Geophysics, **76**, no. 6, H1–H18, doi: 10.1190/geo2010-0039.1.

van der Neut, J., and J. Thorbecke, 2009, Resolution function for controlled-source seismic interferometry: A data-driven diagnosis: 79th Annual International Meeting, SEG, Expanded Abstracts, 4090–4094.

van Manen, D.-J., A. Curtis, and J. O. Robertsson, 2006, Interferometric modeling of wave propagation in inhomogeneous elastic media using time reversal and reciprocity: Geophysics, **71**, no. 4, SI47–SI60, doi: 10.1190/1.2213218.

Wapenaar, C., M. Dillen, and J. Fokkema, 2001, Reciprocity theorems for electromagnetic or acoustic one-way wave fields in dissipative inhomogeneous media: Radio Science, **36**, 851–863, doi: 10.1029/2000RS002394.

Wapenaar, C. P. A., and J. L. T. Grimbergen, 1996, Reciprocity theorems for one-way wavefields: Geophysical Journal International, **127**, 169–177, doi: 10.1111/j.1365-246X.1996.tb01542.x.

Wapenaar, K., 1998, Reciprocity properties of one-way propagators: Geophysics, **63**, 1795–1798, doi: 10.1190/1.1444473.

Wapenaar, K., 2004, Retrieving the elastodynamic Green's function of an arbitrary inhomogeneous medium by cross correlation: Physical Review Letters, **93**, 254301, doi: 10.1103/PhysRevLett.93.254301.

Wapenaar, K., F. Broggini, E. Slob, and R. Snieder, 2013, Three-dimensional single-sided Marchenko inverse scattering, data-driven focusing, Green's function retrieval, and their mutual relations: Physical Review Letters, **110**, 084301, doi: 10.1103/PhysRevLett.110.084301.

Wapenaar, K., J. Thorbecke, and D. Draganov, 2004, Relations between reflection and transmission responses of three-dimensional inhomogeneous media: Geophysical Journal International, **156**, 179–194, doi: 10.1111/j.1365-246X.2003.02152.x.

Wapenaar, K., J. Thorbecke, and J. van der Neut, 2016, A single-sided homogeneous Green's function representation for holographic imaging, inverse scattering, time-reversal acoustics and interferometric Green's function retrieval: Geophysical Journal International, **205**, 531–535, doi: 10.1093/gji/ggw023.

Wapenaar, K., J. Thorbecke, J. van der Neut, F. Broggini, E. Slob, and R. Snieder, 2014, Marchenko imaging: Geophysics, **79**, no. 3, WA39–WA57, doi: 10.1190/geo2013-0302.1.